Volume 17
Number 18
21 September 2024
Pages 6423–6858

Energy & Environmental Science

rsc.li/ees

ISSN 1754-5706

ROYAL SOCIETY OF CHEMISTRY

PAPER

Wei Zhang, Chunyang Miao, Weibing Lu, ZhengMing Sun *et al.*
Ultra-thin amphiphilic hydrogel electrolyte for flexible zinc-ion paper batteries

Energy & Environmental Science

ROYAL SOCIETY OF CHEMISTRY

PAPER

View Article Online
View Journal | View Issue

Cite this: *Energy Environ. Sci.*, 2024, **17**, 6507

Ultra-thin amphiphilic hydrogel electrolyte for flexible zinc-ion paper batteries†

Huan Xia,‡[a] Wei Zhang, ‡*[a] Chunyang Miao, *[b] Hao Chen,[c] Chengjie Yi,[a] Yihan Shang,[d] Tao Shui,[a] Xin Cao,[a] Jiacheng Liu,[e] Song-Zhu Kure-Chu,[e] Feifei Liang,[f] Nosipho Moloto, [g] Yipeng Xiong,[a] Takehiko Hihara,[e] Weibing Lu*[c] and ZhengMing Sun *[a]

Received 7th May 2024,
Accepted 12th July 2024

DOI: 10.1039/d4ee01993h

rsc.li/ees

Hydrogel electrolytes are the ideal platform to construct flexible zinc-ion batteries. However, they usually require immersion in salt solutions to the swollen state for high ion transportation, resulting in a decreased energy density and poor interface adhesion. Herein, we developed a hydrophobic–hydrophilic dual phase stabilization strategy to crosslink polymer membranes into hydrogels based on solvent displacement. The hydrophobic and rigid polyacrylonitrile (PAN) network effectively restricts the swelling behavior of the hydrophilic polyvinyl alcohol (PVA) network, forming an interconnected amphiphilic hydrogel (C-PVA/PAN) with a thickness of only 20 μm even after swelling. The Zn||C-PVA/PAN||Zn symmetric cell cycling tests demonstrate stable performance exceeding 3500 hours without zinc dendrite formation. Molecular dynamics (MD) simulations also corroborate the ability of the C-PVA/PAN hydrogel electrolyte to facilitate uniform zinc deposition. Additionally, paper-like Zn||C-PVA/PAN||$NH_4V_4O_{10}$ batteries with a thickness of only 82 μm exhibit remarkable cycling performance (180 mA h g^{-1} after 3000 cycles at 20 A g^{-1}) and can be folded using the Miura folding technique, significantly enhancing areal energy density. This work presents a facile strategy for designing ultra-thin hydrogel electrolytes, paving the way for powering next-generation flexible electronics through paper-like batteries.

Broader context

Hydrogel electrolytes provide an optimal foundation for the fabrication of flexible zinc-ion batteries. Nonetheless, conventional approaches often necessitate immersion in salt solutions to achieve a swollen state for enhanced ion transportation, albeit at the cost of diminished energy density and suboptimal interface adhesion. In this study, we propose a novel hydrophobic–hydrophilic dual-phase stabilization strategy aimed at crosslinking polymer membranes into hydrogels *via* solvent displacement. The integration of a hydrophobic and rigid polyacrylonitrile (PAN) network effectively mitigates the swelling tendencies of the hydrophilic polyvinyl alcohol (PVA) network. This results in a thin, 20 μm, interconnected amphiphilic hydrogel (C-PVA/PAN) with exceptional stability, as demonstrated by over 3500 hours of symmetric cell cycling without zinc dendrite. Molecular dynamics simulations confirm its effectiveness in promoting uniform zinc deposition. Moreover, paper-like batteries using C-PVA/PAN hydrogel, with a thickness of 82 μm, showcases outstanding cycling performance, achieving 180 mA h g^{-1} after 3000 cycles at 20 A g^{-1}. Notably, these batteries can be seamlessly folded using the Miura folding technique, significantly augmenting their areal energy density. This work introduces a straightforward approach for fabricating ultra-thin hydrogel electrolytes, thereby opening avenues for empowering next-generation flexible electronics through the utilization of paper-like batteries.

[a] *School of Materials Science and Engineering, Southeast University, Nanjing, 211189, China. E-mail: w69zhang@seu.edu.cn, zmsun@seu.edu.cn*
[b] *Jiangsu National Synergetic Innovation Center for Advanced Materials, Key Laboratory of Flexible Electronics and Institute of Advanced Materials, Nanjing Tech University, Nanjing, 211816, China. E-mail: iamcymiao@njtech.edu.cn*
[c] *Center for Flexible RF Technology, State Key Lab of Millimeter waves, School of Information Science and Engineering, Southeast University, Nanjing, 210018, China. E-mail: wblu@seu.edu.cn*
[d] *School of Electrical and Electronic Engineering, Nanyang Technological University, Singapore, 639798, Singapore*
[e] *Department of Materials Function and Design, Nagoya Institute of Technology, Gokiso-cho, Showa-ku, Nagoya, Aichi, 4668555, Japan*
[f] *Contemporary Amperex Technology Co., Ltd., Ningde, 352100, China*
[g] *Molecular Science Institute, School of Chemistry, University of the Witwatersrand, Private Bag 3, Wits, 2050, South Africa*

† Electronic supplementary information (ESI) available. See DOI: https://doi.org/10.1039/d4ee01993h

‡ Huan Xia and Wei Zhang contributed equally to this work.

1. Introduction

Motivated by the escalating demand for powering flexible electronics and wearable devices,[1,2] the development of flexible energy storage systems has become a focal point.[3,4] Zinc-ion batteries (ZIBs) have emerged as an exceptionally promising solution due to their high safety standards and environmental friendliness.[5,6] Utilizing hydrogel materials as both electrolyte carrier and structure support is considered as an effective strategy to construct flexible ZIBs.[7–9] However, conventional hydrogel electrolytes including polyacrylamide (PAM)[10] and polyvinyl alcohol (PVA)[11] hydrogels, demand immersion in salt solutions to attain a swollen state for efficient zinc-ion transportation. Unfortunately, the swollen state not only thickens the electrolyte, diminishes the energy density of ZIBs, but also leads to poor adhesion at the electrode–electrolyte interface.[12–14] Additionally, inherent issues with hydrogen evolution reaction (HER) and oxygen evolution reaction (OER) are exacerbated by increasing water content,[15–17] jeopardizing the long-term stability of flexible ZIBs.

Achieving elevated ion conductivity in hydrogel electrolytes with low water content involves strategically endowing the hydrogel polymer skeleton with ionic conducting capability.[13,18] Polar functional groups such as ether bonds,[19] hydroxyl groups,[20] and sulfonic acid groups[21] are introduced into the framework to enhance ion transport, resulting in an improved ion conductivity more than 10 mS cm^{-1}.[13] However, these polymer chains, capable of facilitating the transmission of both zinc ions and anions, could lead to the concentration polarization of anions and uneven zinc deposition.[22–24] Single-zinc-ion conductive hydrogel electrolytes have been developed to achieve directed zinc-ion transport under low water content and mitigate the issue of anion movement.[12,25,26] For example, the slide-ring structure with anionic spatial confinement[12] and the covalent organic frameworks channels with enhanced zinc ion affinity[25] could result in a zinc ion transfer number larger than 0.9, while reducing water content of the hydrogel electrolytes to 60%.[12,25] Nevertheless, their thicknesses still remain at a millimeter scale, posing a challenge for practical applications in many flexible electronic devices, such as electronic skins,[27] flexible pacemakers[28] and oximeters[29] with a thickness ranging from 100 μm to 300 μm. To further decrease the thickness of hydrogel electrolytes, natural polysaccharides (Xanthan gum[30] and Guar gum[31]) have been engineered into a thickness of 300 μm. However, their mechanical performance, particularly toughness, are compromised due to their high crystallinity and week crosslinking *via* hydrogen bonding.[32–34] This renders them susceptible to zinc dendrite penetration, especially as the thickness decreases.

Classical rigid polymer fiber membranes possess thicknesses within the sub-hundred micrometer range and excellent mechanical properties, effectively preventing dendritic penetration.[35,36] Nonetheless, these membranes lack the inherent water-retaining properties of hydrogel electrolytes and may encounter leakage during bending and folding processes.[37,38] Therefore, the successful construction of flexible electrolytes appears to rely on integrating the mechanical properties of the polymer membrane with the water-retaining capacity of hydrogel materials.[39,40] For the stability of the electrolyte, it is essential to ensure uniform distribution of the rigid network and the hydrophilic network within the system. However, polymer fiber membranes typically have low surface energy and hydrophobic surfaces, which could disrupt the stable hydrogen bonds formed between the hydrophilic hydrogel network and water, leading to a decrease in the polymer solubility and even precipitation.[41,42]

Herein, we have developed a hydrophobic–hydrophilic phase stabilization strategy to crosslink polymer membranes into hydrogels based on solvent displacement. Such design endows the hydrogel structure with dual polymer networks, where the hydrophobic network is composed of physically entangled polyacrylonitrile (PAN) fibers prepared *via* electrospinning, and the hydrophilic network consists of polyvinyl alcohol (PVA) polymer chains chemically crosslinked with epichlorohydrin (ECH). The hydrophobic and rigid PAN network effectively restricts the swelling behavior of the hydrophilic PVA network, forming an interconnected amphiphilic hydrogel (C-PVA/PAN) with a thickness of only 20 μm even after swelling. The hydrogel skeletons enriched with polar functional groups are beneficial to zinc ions transmission and possess a high ionic conductivity of 17.4 mS cm^{-1}. The Zn||C-PVA/PAN||Zn symmetric cell demonstrated stable cycling exceeding 3500 h at 1 mA cm^{-2} without generating zinc dendrite. MD simulations also confirm the capability of the C-PVA/PAN hydrogel electrolyte to enable uniform zinc deposition on the surface of zinc foil. Moreover, owing to the exceptionally thin nature of the hydrogel electrolyte, the Zn||C-PVA/PAN||$NH_4V_4O_{10}$ batteries could be assembled with a thickness of only 82 μm, thinner than a piece of a standard A4 paper sheet (104 μm, ISO 216). The paper-like ZIBs manifested a remarkable cycling performance of 180 mA h g^{-1} after 3000 cycles at 20 A g^{-1}. Additionally, the paper-like ZIBs can be folded and unfolded by the Miura folding technique, where 18 individual paper-like battery units can simultaneously expand. Through this approach, the areal energy density of the ZIBs is enhanced by a factor of 18, significantly facilitating the portability of batteries within constrained spaces. This work demonstrates a facile strategy of designing ultra-thin hydrogel electrolytes, aimed at providing power for future ultrathin flexible electronics through flexible batteries.

2. Results and discussion

As elucidated in Fig. 1, the preparation of C-PVA/PAN hydrogel electrolyte involves three steps. In the initial step, a physically intertwined polymer PVA/PAN membrane (P-PVA/PAN) was fabricated by electrospinning a dimethyl formamide (DMF) solution containing 50 wt% PVA and 50 wt% PAN. Then, the PVA chains in the P-PVA/PAN network was crosslinked *via* ECH, forming glycidyl ether through dialcohol groups (Fig. 1 and Fig. S1, ESI†). Finally, the hydrogel electrolyte was obtained by

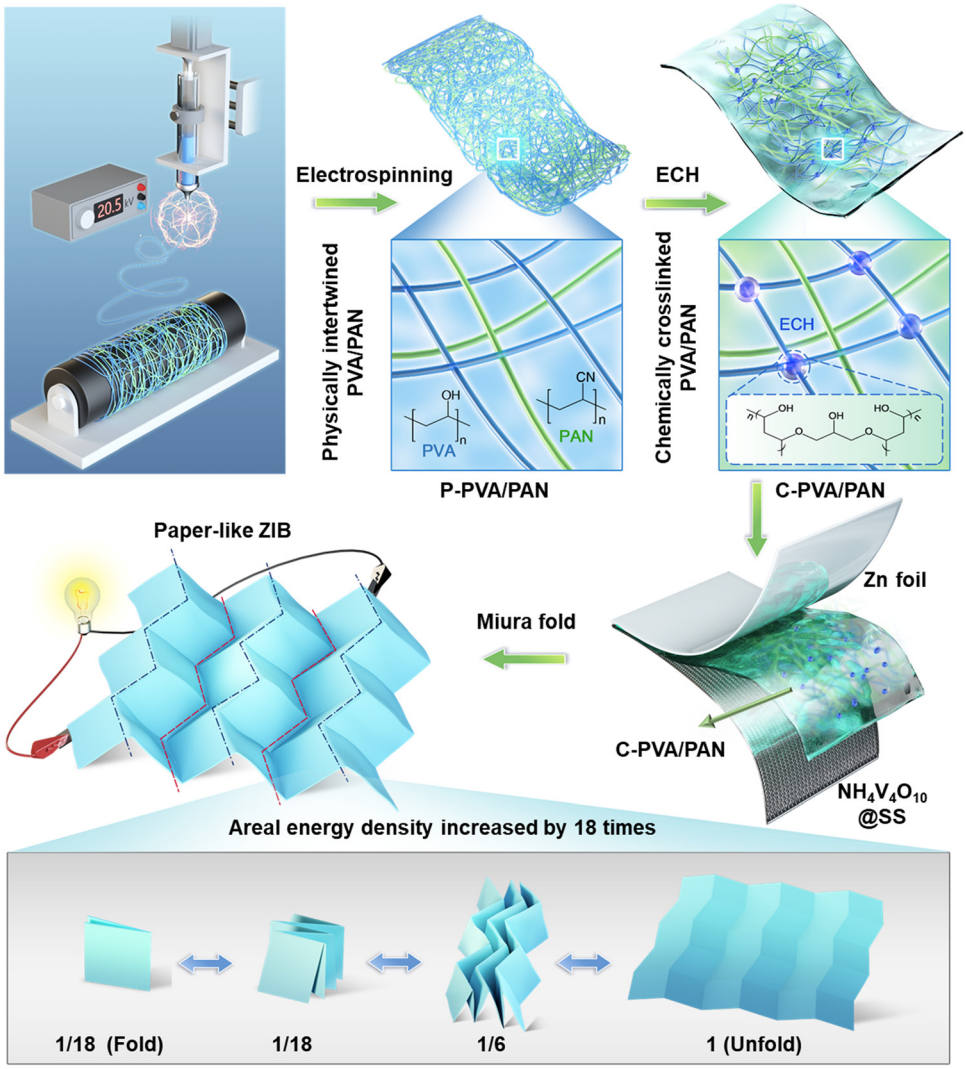

Fig. 1 Schematic illustration of the preparation for C-PVA/PAN hydrogel with dual hydrophobic–hydrophilic polymer networks and paper-like ZIBs with Miura folding technique, the hydrophobic network is composed of physically entangled PAN fibers prepared *via* electrospinning, and the hydrophilic network consists of PVA polymer chains chemically crosslinked with ECH.

immersing the solution of zinc trifluoromethanesulfonate ($ZnOTf_2$). This approach not only ensures the establishment of a robust interconnected network within the C-PVA/PAN hydrogel film, but also dynamically constrains the swelling of hydrogels by the rigid network, enabling the ultra-thin design.

Even immersed into saturation, the thickness of the C-PVA/PAN electrolyte remains nearly unchanged and exhibits a thickness of only 20 μm (thinner than a standard A4 paper, Fig. 2(a) and Fig. S2, S3, ESI†), yet the mass increases by 200%. This phenomenon can be attributed to the fact that the hydrophilic PVA network is limited by the rigid PAN network which is difficult to produce large deformation during the process of swelling (Fig. 2(b) and (c)). In contrast, the pure PVA hydrogel film could swell to a thickness of 2.403 mm due to the absence of a constraint network. Due to the limitations of the electrospinning machine, the maximum size of the hydrogel electrolyte is 30 cm × 20 cm (Fig. S4, ESI†). Over the course of 7 days, the water retention ratio of the C-PVA/PAN hydrogel is significantly higher than that of the P-PVA/PAN hydrogel (Fig. S5, ESI†), indicating that the chemical crosslinking enhances the hydrogel's water retention capability. As shown in the SEM image of Fig. 2(d), the P-PVA/PAN film exhibits a random distribution of fibers with diameters ranging from 400 to 600 nm. The C-PVA/PAN still maintains the porous structure (Fig. 2(e)) with pore diameters ranging from 1 to 3 μm. Fig. 2(f) provides the FTIR spectra of the hydrogel electrolyte both pre (blue) and post (purple) crosslinking. The carbon–oxygen bond stretching vibration (–C–O–H) characteristic peak in the PVA chain located at 1087 cm^{-1}. Following introduction of ECH, this peak undergoes a shift to 1079 cm^{-1} due to the formation of glycidyl ether. Additionally, a new characteristic peak attributing to the ether bond (C–O–C) stretching vibration of glycidyl ether emerges at 1051 cm^{-1} (Fig. 2(f)). A comparative analysis of the mechanical properties between P-PVA/PAN and

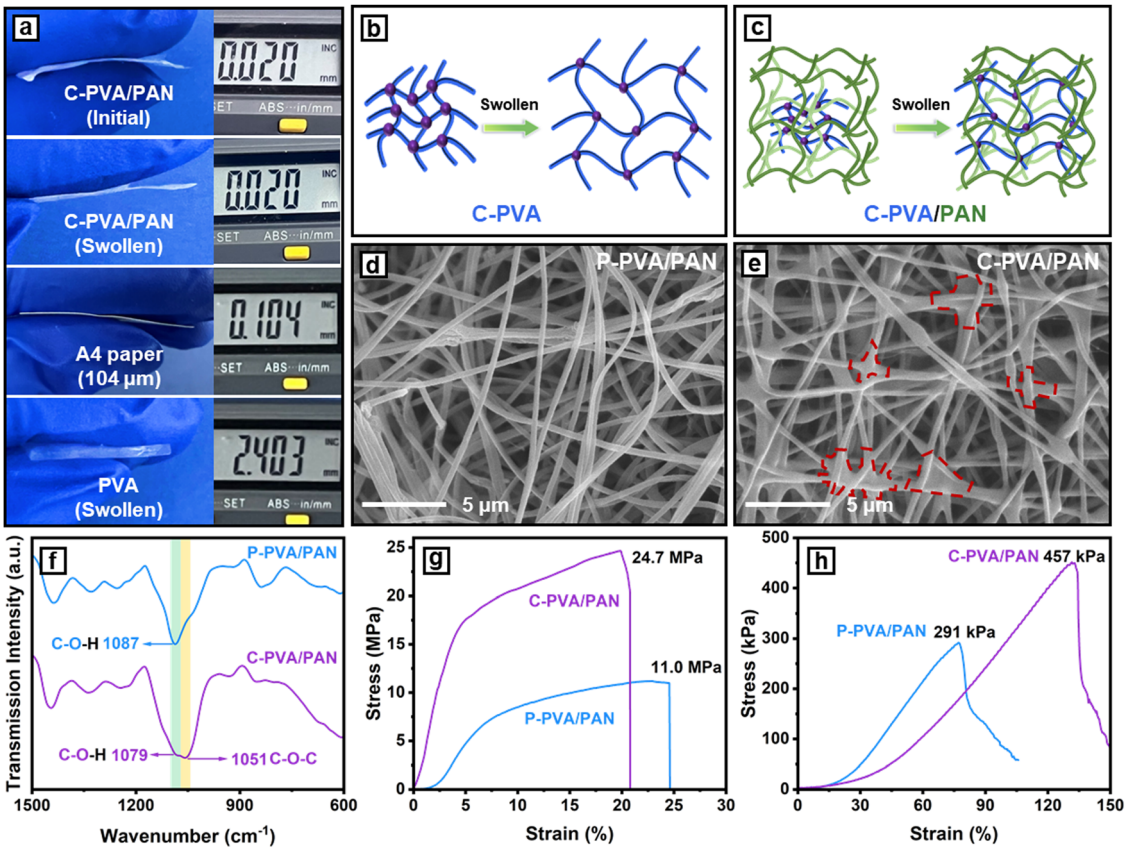

Fig. 2 (a) Thickness measurement of the C-PVA/PAN hydrogel (initial), C-PVA/PAN hydrogel (swollen), A4 paper, and PVA hydrogel (swollen). Swelling schematic illustration of (b) PVA and (c) C-PVA/PAN hydrogel. Scanning electron microscopy (SEM) images of (d) the P-PVA/PAN film and (e) the C-PVA/PAN hydrogel film. (f) Fourier-transform infrared spectroscopy (FTIR) spectra of the P-PVA/PAN film and the C-PVA/PAN hydrogel film. (g) Representative tensile stress–strain curves and (h) puncture stress–strain curves for the P-PVA/PAN film and the C-PVA/PAN hydrogel film.

C-PVA/PAN further confirmed the successful crosslinking of the PVA polymer chains. The P-PVA/PAN exhibits a tensile strength of only 11.0 MPa, which experiences a remarkable 282% increase to 24.7 MPa after crosslinking, and the puncture strength also increases from 291 kPa to 457 kPa (Fig. 2(h)).

The electrochemical stability window of the C-PVA/PAN hydrogel electrolyte was determined by linear sweep voltammetry (LSV) curves at a scan rate of 0.1 mV s^{-1} (Fig. 3(a)). The P-PVA/PAN exhibits a noticeable increase in current at 1.7 V, indicating the onset of electrolyte decomposition at this point. In contrast, the C-PVA/PAN hydrogel electrolyte demonstrates a similar surge in current above 2 V. This can be attributed to the introduction of ether bonds from ECH, which can form hydrogen bonding with water, leading to the formation of more bound water in the hydrogel.[43,44] Molecular dynamics (MD) simulations result also indicate that due to the introduction of ether bonds, the C-PVA/PAN hydrogel exhibits a stronger binding capacity for water molecules (Fig. S6 and S7a, ESI†). This observation is similarly supported by differential scanning calorimetry (DSC) testing, where the broad endothermic peak corresponding to water absorption shifts from 98.7 °C to 102.7 °C (Fig. S7b, ESI†), indicating the presence of more bound water. Compared to free water, the decomposition of bound water requires a higher decomposition voltage. The transference number measured using the classic Bruce–Vincent method indicates that the transference number ($t_{Zn^{2+}}$) of the C-PVA/PAN hydrogel electrolyte is 0.64, while the transference number before crosslinking, P-PVA/PAN, is 0.61 (Fig. S8, ESI†). This indicates that zinc ion migration remains predominant before and after crosslinking. As depicted in Fig. 3(b), the ionic conductivity of both P-PVA/PAN and C-PVA/PAN electrolytes are determined based on electrochemical impedance spectroscopy (EIS). Generally, higher crosslinking density in hydrogels leads to increased difficulty in ion transport and lower ionic conductivity.[45] Additionally, in the C-PVA/PAN hydrogel, the introduction of numerous electronegative ether bond functional groups increases the amount of bound water. However, this also results in more active sites for zinc ions within the hydrogel framework.[13,25,46] As a result, the ionic conductivity of C-PVA/PAN remains within the same order of magnitude as that of P-PVA/PAN, and may even slightly increase (17.4 mS cm^{-1}). The activation energy for the C-PVA/PAN hydrogel electrolyte is 0.08 eV, while for the P-PVA/PAN it is 0.10 eV (Fig. S9, ESI†). The lower activation energy indicates that ion migration is easier in the C-PVA/PAN system.

To substantiate the reversible deposition performance of Zn with the C-PVA/PAN hydrogel electrolyte during cycling, constant current polarizations of symmetric cells were investigated.

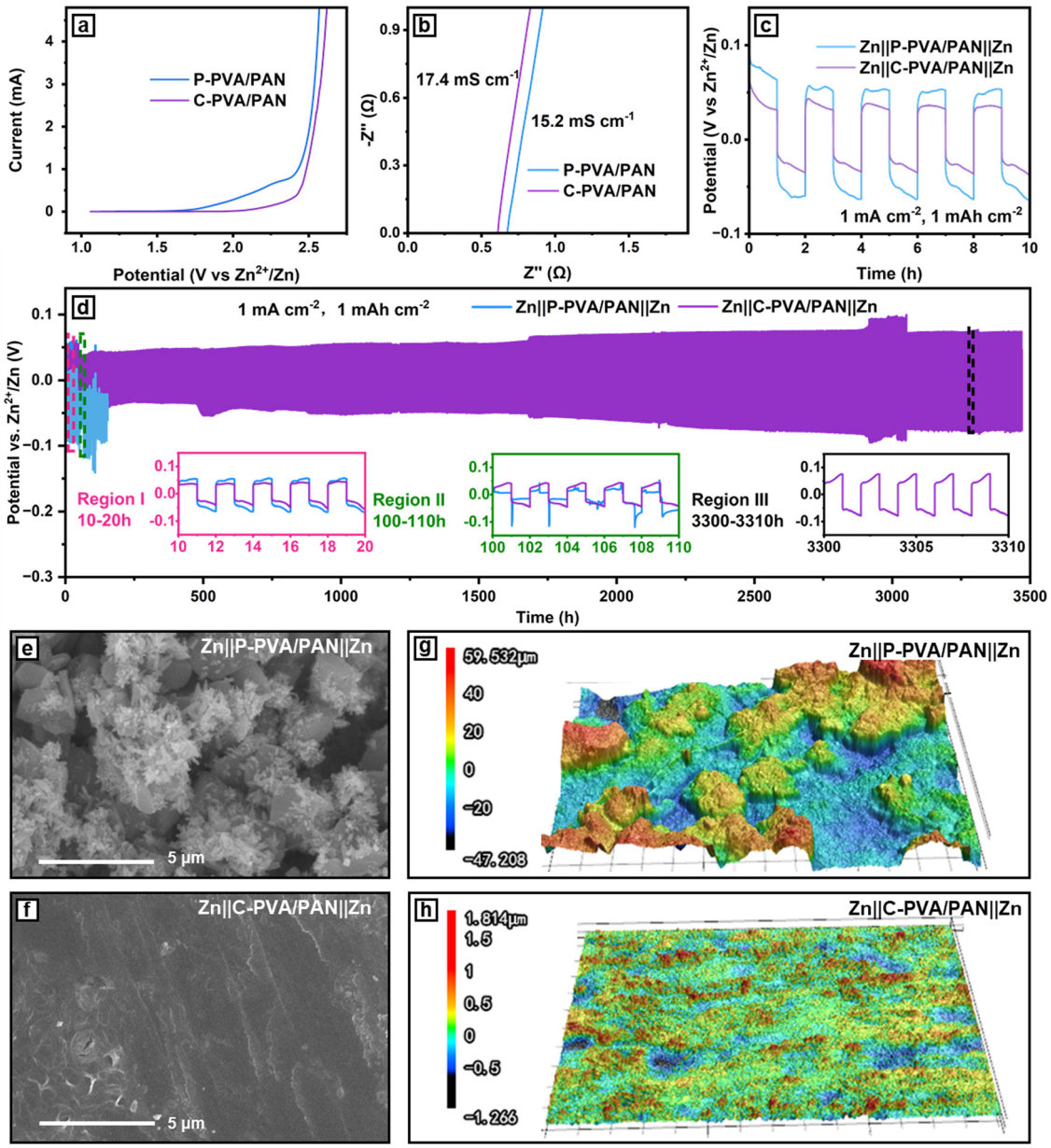

Fig. 3 (a) Linear sweep voltammetry (LSV) curves of the P-PVA/PAN and the C-PVA/PAN hydrogel electrolytes. (b) Electrochemical Impedance Spectroscopy (EIS) spectra of the P-PVA/PAN and the C-PVA/PAN hydrogel electrolyte in the frequency ranges from 100 kHz to 10 mHz. (c) Cycles performance of the Zn||P-PVA/PAN||Zn and the Zn||C-PVA/PAN||Zn symmetric cells at 1 mA cm^{-2} and 1 mA h cm^{-2}. (d) Long cycles performance of the Zn||P-PVA/PAN||Zn and the Zn||C-PVA/PAN||Zn symmetric cells at 1 mA cm^{-2} and 1 mA h cm^{-2}. SEM images of the zinc foil surface after 100 h cycling at 1 mA cm^{-2} using (e) P-PVA/PAN and (f) C-PVA/PAN electrolytes in zinc symmetric cells. Laser confocal microscope images (LCM) of the zinc foil surface after 100 h cycling at 1 mA cm^{-2} using (g) P-PVA/PAN and (h) C-PVA/PAN electrolytes in zinc symmetric cells.

The Zn plating/stripping voltage profile of the symmetric cells with P-PVA/PAN and C-PVA/PAN hydrogel electrolytes at 1 mA cm^{-2} and 1 mA h cm^{-2} are presented in Fig. 3(c) and (d). The Zn||C-PVA/PAN||Zn cell shows a stable polarization voltage for over 3500 h with a smooth voltage profile in each cycle and can stable up to 0.06 V, while the Zn||P-PVA/PAN||Zn cell experiences severe polarization after only 50 cycles due to the formation of zinc dendrites. SEM images of the zinc foil surface after plating/stripping cycles in Zn||Zn symmetric cells with P-PVA/PAN and C-PVA/PAN hydrogel electrolytes at 1 mA cm^{-2} are presented in Fig. 3(e) and (f). The Zn||C-PVA/PAN||Zn cell displays stable cycling for over 100 h, maintaining a smooth zinc metal surface. In contrast, the zinc surface of the Zn||P-PVA/PAN||Zn cell is covered with large lamellar zinc dendrites. Further insight into the deposition and stripping behavior of zinc over a larger area is analyzed by laser confocal microscopy (Fig. 3(g) and (h)). In the system employing C-PVA/PAN electrolyte, zinc deposition on the foil appears remarkably uniform, with minimal variations in zinc thickness (less than 2 μm). In contrast, the system using P-PVA/PAN electrolyte

exhibits a rougher surface, attributed to the presence of zinc dendrites, with the highest zinc dendrite height reaching up to 59 μm.

To visually and effectively observe the dendritic growth process of zinc electrodes with different electrolyte systems, we applied a high current density of 10 mA cm^{-2} to electrochemically deposit zinc on zinc foils using both P-PVA/PAN and C-PVA/PAN electrolytes. The *in situ* deposition results were captured *via* optical microscopy as depicted in Fig. 4(a). In the P-PVA/PAN system, zinc dendrites emerged on the zinc foil after 20 min (Fig. S10, ESI†), progressively growing over time. Conversely, there was no discernible zinc dendritic growth even after 180 min in the C-PVA/PAN system (Fig. 4(b)). The dynamic growth of zinc dendrites is also elaborated in Movies S1 and S2 (ESI†).

To comprehensively elucidate the role of C-PVA/PAN in facilitating Zn deposition, the mathematical model fitting of the Zn deposition behaviors on the Zn electrode with P-PVA/PAN or C-PVA/PAN electrolyte was further carried out *via* the MD simulations (Fig. 4(c) and (d)). Under the influence of an electric field, zinc ions undergo deposition and reduction on the surface of the Zn foil. Initially, the zinc foil possesses a smooth and uniform surface. Upon deposition of zinc ions from the P-PVA/PAN electrolyte onto the zinc foil surface, conspicuous irregularities in deposition are observed. However, in the case of the C-PVA/PAN system, the zinc surface exhibits comparatively smooth characteristics in its final state. This phenomenon can be explained by the migration of zinc under the influence of an electric field within the P-PVA/PAN system, which simultaneously triggers the movement of certain PVA chains, causing the compression of initially uniformly distributed channels for zinc migration. Consequently, uneven zinc deposition occurs, exacerbated by the "tip effect" where zinc dendrites tend to rapidly form at protrusions,[47,48] thus

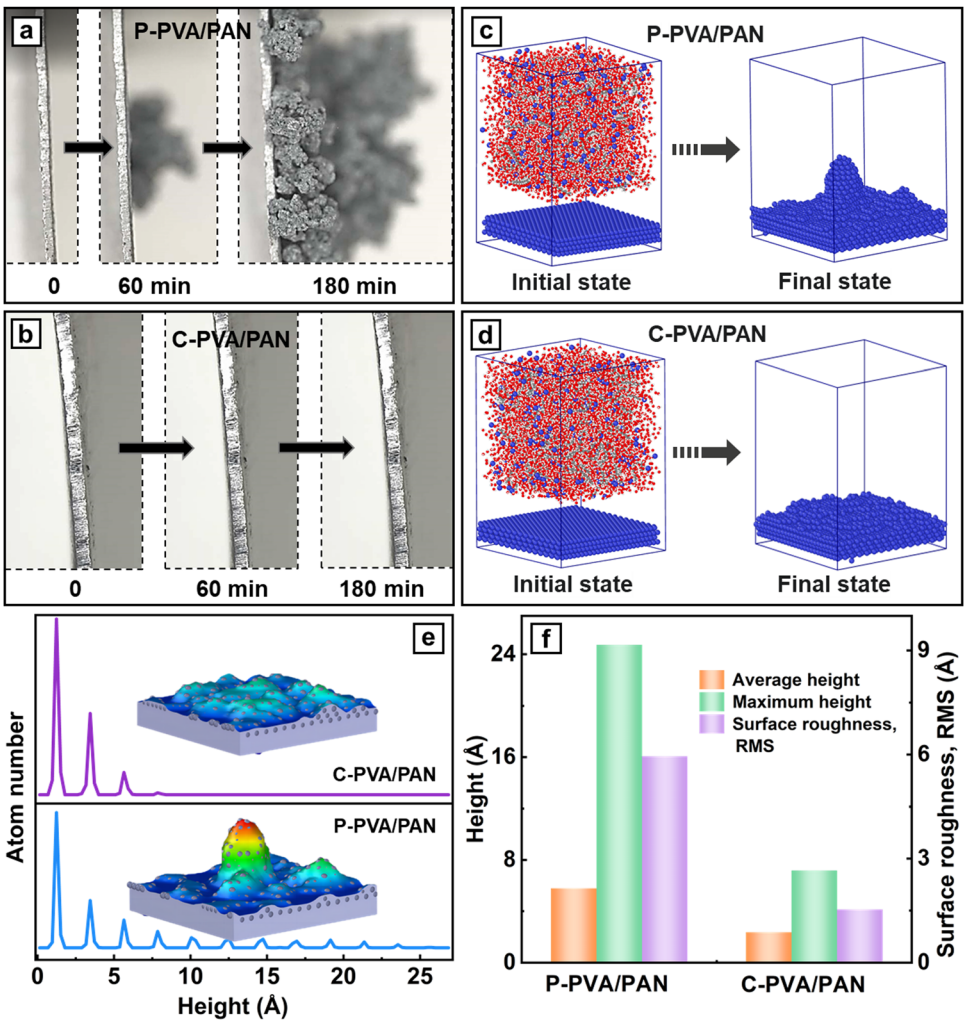

Fig. 4 The *in situ* optical images of the Zn plating behaviors with (a) P-PVA/PAN and (b) C-PVA/PAN electrolyte at 10 mA cm^{-2}. Molecular dynamics simulation models of Zn anode with (c) P-PVA/PAN or (d) C-PVA/PAN electrolyte. (e) The number of Zn atoms indicating the distribution of the deposited atoms along height in different electrolytes at the final sate, quantitatively reflecting the compactness of the deposited atoms and the morphology of the deposition. The inset images showing the comparison of the surface morphology and corresponding surface height of the Zn foil at the final state of the simulation in different electrolytes. (f) Comparison of the deposition height and surface roughness of the Zn foil in different electrolytes at the final sate.

accelerating dendrite growth. In contrast, the structure of the PVA network in the C-PVA/PAN system is less susceptible to movement due to covalent cross-linking, thereby maintaining the uniform deposition of zinc. Moreover, the incorporation of ECH into the C-PVA/PAN system introduces numerous ether functional groups into the original structure. Oxygen molecules from these ether bonds preferentially adsorb onto the surface of the zinc foil,[49] thereby enhancing its ability to establish a uniform electric field. As a result, the deposition process on the zinc surface becomes more uniform and consistent.

Subsequently, to qualitatively compare the morphology of Zn deposits on the zinc foil in the two electrolyte systems, the deposition height, surface roughness, and histogram of the distribution of deposited atoms along the height direction of the zinc foil surface were conducted (Fig. 4(e) and (g)). Upon analyzing the histogram of the distribution of deposited Zn atoms along the height direction of the zinc foil surface, it was observed that in the C-PVA/PAN system model (the purple line in Fig. 4(e)), the fluctuation of the number of deposited Zn atoms remains relatively stable with the increase in deposition height. This observation suggests that Zn atoms are deposited in an orderly and compact manner. In contrast, in the P-PVA/PAN electrolyte case (the blue line in Fig. 4(e)), the number of deposited Zn atoms exhibits a noticeable downward trend as the deposition height increases, indicating that the arrangement of deposited Zn atoms is chaotic and disordered. This trend aligns with the surface morphology of the zinc foil (insets of Fig. 4(e)).

Furthermore, in the C-PVA/PAN electrolyte model, a higher concentration of deposited Zn atoms is observed within a narrow height range (approximately 0–8 Å), whereas in the P-PVA/PAN electrolyte model, fewer deposited Zn atoms are stacked to a greater height (approximately 0–25 Å, Fig. 4(f)). This observation suggests that Zn deposition is more compact and uniform on the surface of zinc foil in the C-PVA/PAN hybrid electrolyte model, while in the P-PVA/PAN electrolyte model, zinc ions are more prone to forming dendritic-like and non-compact protrusions. Additionally, a quantitative comparison of the surface roughness of the zinc plate after Zn plating was conducted in the two electrolyte models (Fig. 4(f)). The results indicate that C-PVA/PAN electrolytes effectively promote uniform Zn deposition, resulting in lower surface roughness. This finding is consistent with the experimental results mentioned earlier. Overall, the experimental and theoretical calculation results presented herein support the conclusion that C-PVA/PAN hydrogel electrolytes facilitate stable Zn plating/stripping processes on zinc metal surfaces, thereby mitigating dendrite proliferation.

Vanadium-based materials, such as V_2O_5, vanadates, and vanadium oxide composites,[50–53] although limited in cycling stability at low current densities, typically exhibit multivalent state transition capabilities. This allows them to achieve high theoretical capacity and energy density in zinc-ion storage. Additionally, due to the rapid migration of zinc ions within vanadium-based materials, they generally display good rate performance, making them suitable for high-power applications. In summary, vanadium-based materials are highly advantageous as flexible battery cathode materials for wearable devices. To evaluate the electrochemical performance of the C-PVA/PAN hydrogel electrolyte in flexible ZIBs, we fabricated an intercalation-type cathode materials $NH_4V_4O_{10}$ with high theoretical ion diffusion and storage ability to assemble ZIBs. Fig. S11 (ESI†) demonstrated the characteristic pattern of $NH_4V_4O_{10}$ (PDF#00-056-1359) in the X-ray diffraction (XRD) profile. The SEM image shows that $NH_4V_4O_{10}$ crystallizes into uniform nanorod morphology with a diameter of approximately 100 nm and a length of around 500 nm (Fig. S12, ESI†). Flexible ZIBs with the C-PVA/PAN hydrogel electrolyte were assembled into sandwich structures, utilizing $NH_4V_4O_{10}$ @stainless steel mesh ($NH_4V_4O_{10}$ @SS) as the cathode and zinc plates as the anode (Fig. S13, ESI†). Cyclic voltammograms (CV) profiles were then employed to study charge–discharge intervals of the battery. As displayed in Fig. S14 (ESI†), there are six pairs of redox peaks located at 1.48/1.29, 1.17/0.92, 0.78/0.86, 0.71/0.76,0.52/0.50, and 0.45/0.40 V during cycle for Zn||C-PVA/PAN||$NH_4V_4O_{10}$, which suggests a multistep reaction consistent with the previous reports.[54,55] The Zn||C-PVA/PAN|| $NH_4V_4O_{10}$ battery exhibits a high initial capacity of 501 mA h g^{-1} at 0.1 A g^{-1} with an open-circuit potential of 1.195 V (Fig. 5(a)). After 50 cycles, the Zn||C-PVA/PAN|| $NH_4V_4O_{10}$ battery demonstrates outstanding cycling performance with almost no capacity attenuation at 0.1 A g^{-1} (Fig. 5(b)). In contrast, the control Zn||P-PVA/PAN||$NH_4V_4O_{10}$ battery exhibits a capacity retention of only 85.3% after 50 cycles at 0.1 A g^{-1}. With increasing current densities, the flexible Zn||C-PVA/PAN||$NH_4V_4O_{10}$ battery reveals average discharge capacities of 498, 479, 451, 425, 392, 267, 192, and 100 mA h g^{-1} at 0.2, 0.5, 1, 2, 5, 10, 20, and 30 A g^{-1} (Fig. 5(c)), significantly surpassing those of the Zn||P-PVA/PAN||$NH_4V_4O_{10}$ batteries. Furthermore, the Zn||C-PVA/PAN|| $NH_4V_4O_{10}$ battery maintains a discharge specific capacity of 180 mA h g^{-1} even after 3000 cycles at a current density of 20 A g^{-1} (Fig. 5(d)).

A comparison was made with state-of-the-art flexible ZIBs utilizing hydrogel electrolytes. The specific capacity at a low current density and the thickness of hydrogel electrolytes were plotted in Fig. 5(e) and (f) (also summarized in Tables S1 and S2, ESI†).[12,30,31,47,56–81] Notably, our ZIB demonstrated the highest specific capacity at low current densities of 0.1, 0.2, and 0.5 A g^{-1}. Additionally, it can achieve the highest specific capacity even with the minimum thickness of the hydrogel electrolyte. Even at the millimeter level of thickness of the hydrogel electrolyte, the specific capacity remains the highest value, outperforming most of the current hydrogel-based ZIBs. The comparison of energy density and power density (Fig. 5(e)) further highlights the performance of our ZIB over other systems (Zn||LPH||MgVO,[66] Zn||CMCNa||KVO,[82] Zn||PAM-ChNF||VO_2,[10] Zn||PVA||Od-NVO,[83] Zn||CH/D/Fe||P-V_2O_5,[84] Zn||gelatin||MnO_2[85]). The Zn||P-PVA/PAN||$NH_4V_4O_{10}$ batteries exhibited an exceptional energy density of up to 420 W h kg^{-1} and an impressive power density of 28.8 kW kg^{-1}.

Benefiting to the ultra-thin hydrogel electrolyte design, the unencapsulated sandwich-structured ZIB achieves a remarkable thickness of only 82 μm (Fig. S15, ESI†), thinner than a standard A4 paper sheet (Fig. S2, ESI†). Even after encapsulation,

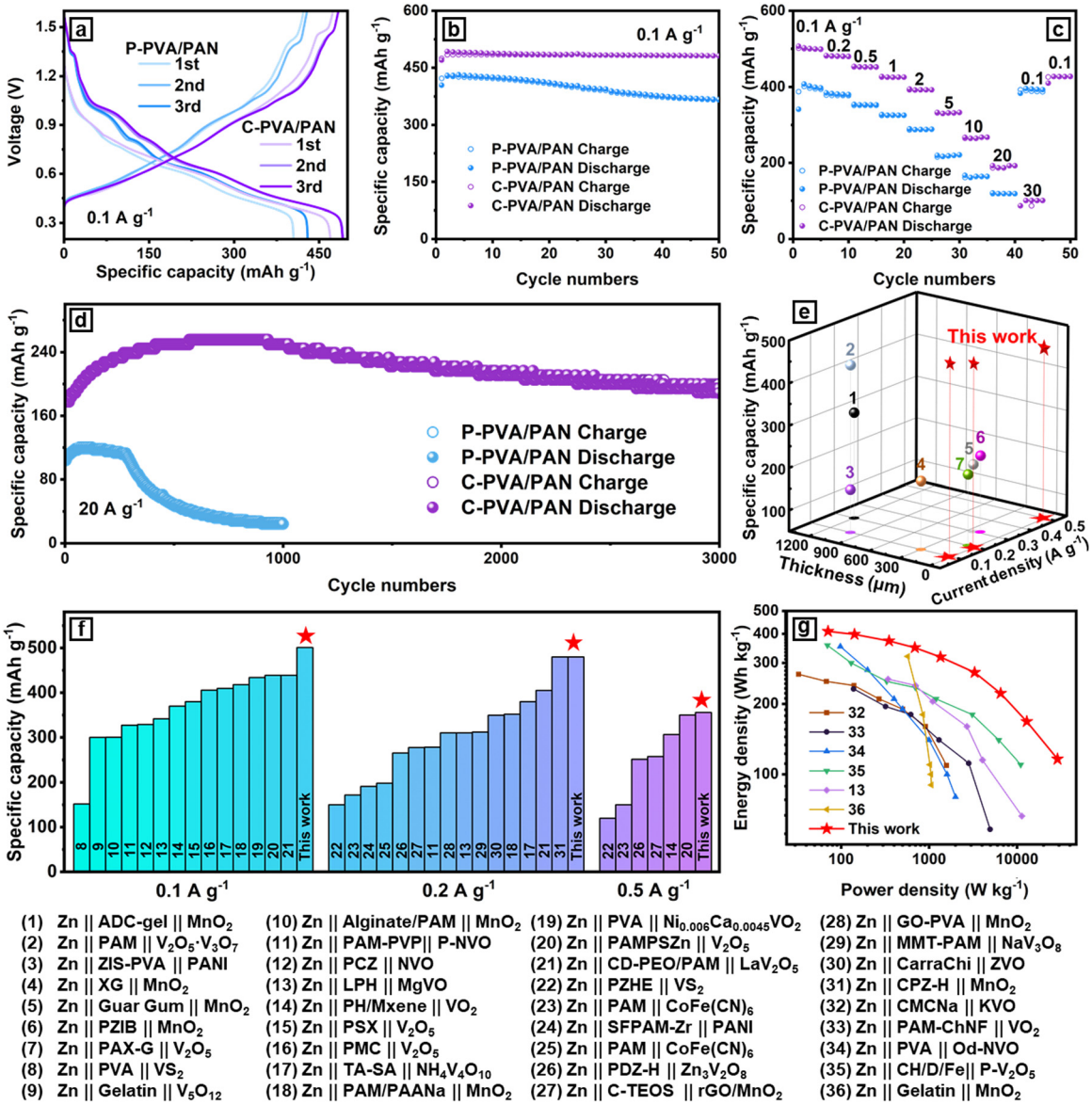

(1) Zn || ADC-gel || MnO_2
(2) Zn || PAM || $V_2O_5{\cdot}V_3O_7$
(3) Zn || ZIS-PVA || PANI
(4) Zn || XG || MnO_2
(5) Zn || Guar Gum || MnO_2
(6) Zn || PZIB || MnO_2
(7) Zn || PAX-G || V_2O_5
(8) Zn || PVA || VS_2
(9) Zn || Gelatin || V_5O_{12}
(10) Zn || Alginate/PAM || MnO_2
(11) Zn || PAM-PVP|| P-NVO
(12) Zn || PCZ || NVO
(13) Zn || LPH || MgVO
(14) Zn || PH/Mxene || VO_2
(15) Zn || PSX || V_2O_5
(16) Zn || PMC || V_2O_5
(17) Zn || TA-SA || $NH_4V_4O_{10}$
(18) Zn || PAM/PAANa || MnO_2
(19) Zn || PVA || $Ni_{0.006}Ca_{0.0045}VO_2$
(20) Zn || PAMPSZn || V_2O_5
(21) Zn || CD-PEO/PAM || LaV_2O_5
(22) Zn || PZHE || VS_2
(23) Zn || PAM || $CoFe(CN)_6$
(24) Zn || SFPAM-Zr || PANI
(25) Zn || PAM || $CoFe(CN)_6$
(26) Zn || PDZ-H || $Zn_3V_2O_8$
(27) Zn || C-TEOS || rGO/MnO_2
(28) Zn || GO-PVA || MnO_2
(29) Zn || MMT-PAM || NaV_3O_8
(30) Zn || CarraChi || ZVO
(31) Zn || CPZ-H || MnO_2
(32) Zn || CMCNa || KVO
(33) Zn || PAM-ChNF || VO_2
(34) Zn || PVA || Od-NVO
(35) Zn || CH/D/Fe|| P-V_2O_5
(36) Zn || Gelatin || MnO_2

Fig. 5 Electrochemical performance of the flexible Zn||P-PVA/PAN||$NH_4V_4O_{10}$ battery and the Zn||C-PVA/PAN||$NH_4V_4O_{10}$ battery. (a) Galvanostatic charge/discharge profiles at 0.1 A g^{-1}. (b) Cycling performance at 0.1 A g^{-1}. (c) Rate performance at different current densities from 0.1 A g^{-1} to 30 A g^{-1}. (d) Long cycle performance at 20 A g^{-1}. (e) The specific capacity of Zn||C-PVA/PAN|| $NH_4V_4O_{10}$ battery at low current densities and the thickness of C-PVA/PAN hydrogel electrolyte with recently reported hydrogel-based flexible ZIBs. (f) The specific capacity of Zn||C-PVA/PAN|| $NH_4V_4O_{10}$ battery with recently reported hydrogel-based flexible ZIBs at low current densities. (g) The Lagone diagram comparison of the Zn||C-PVA/PAN|| $NH_4V_4O_{10}$ battery with other hydrogel-based flexible ZIBs.

the battery thickness remains a mere 400 μm (Fig. S16, ESI†). These paper-like ZIBs feature an assembly pattern similar to Lego interlocking, allowing various connection and assembly. Both the stacked and flat structures utilize 4 paper-like batteries in series, each with an open-circuit voltage of approximately 1.2 V. The combined voltage of four batteries in series meets the power supply requirements of mainstream smartphones. As showcased in Fig. 6(a), a single battery successfully powers a temperature and humidity sensor. To further underscore the advantages of our paper-like battery in diverse configurations, we selected two representative connection modes—flat layout in series and stacked layout in series—to achieve fast charging for smartphones. Furthermore, the paper-like ZIB can be easily folded and unfolded. By utilizing the Miura folding technique, complex three-dimensional structures can be achieved through simple folding patterns. When folded using this technique, the structure forms distinctive creases and can be unfolded into a parallelogram "grid" with a simple stretch along a single axis. To collapse it back, a push in the opposite direction suffices. Additionally, the creases allow the battery to be stretched and bent without applying excessive stress to the internal components. As shown in Fig. 6(b), the areal energy density can be increased up to 18 times the original value. A temperature and humidity sensor can be operated during the synchronous folding and unfolding process (Fig. 6(b) and

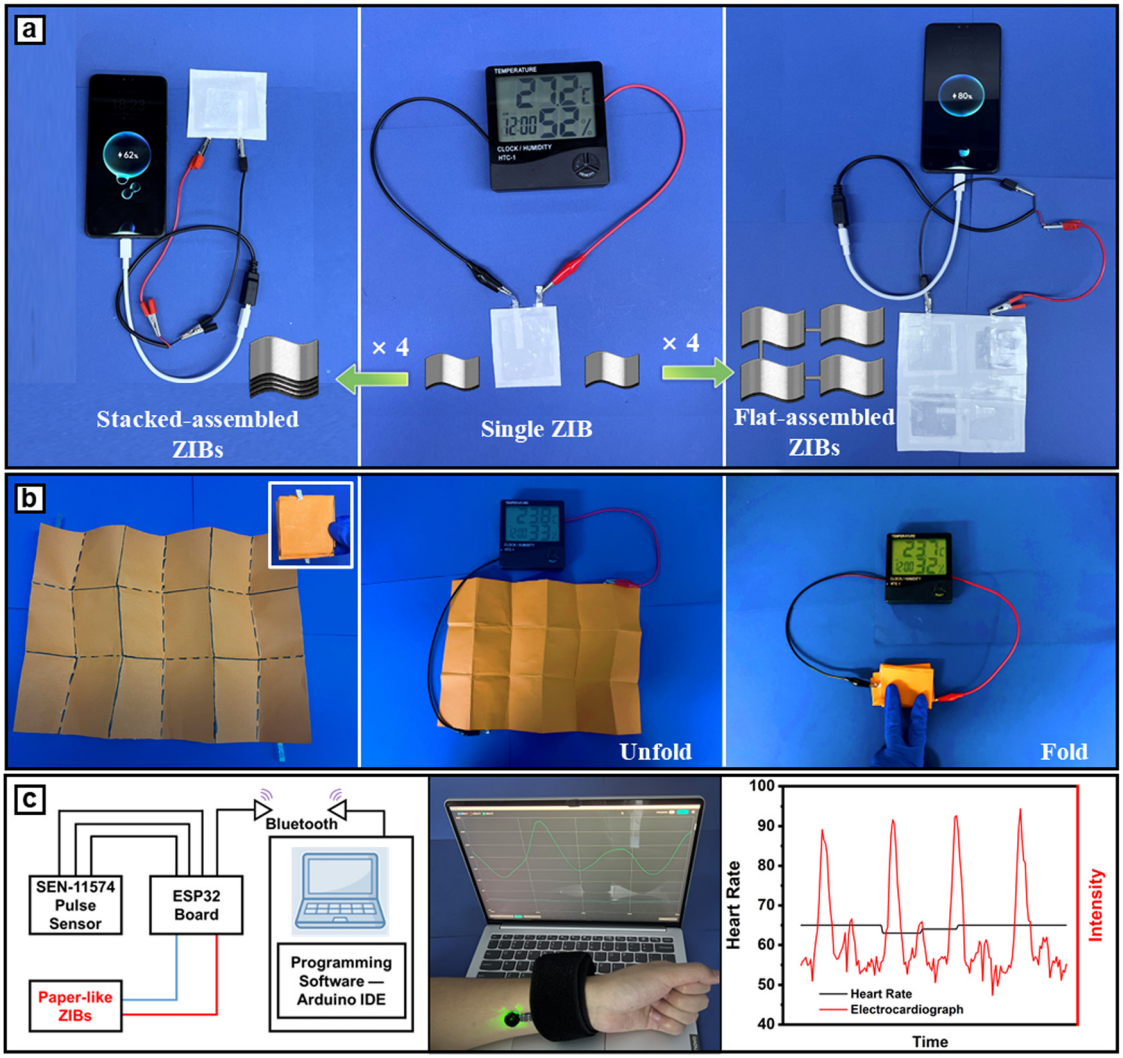

Fig. 6 Applications of the flexible Zn||C-PVA/PAN||$NH_4V_4O_{10}$ paper-like batteries for portable and wearable electronics. (a) A single ZIB for powering a temperature and humidity sensor, four of them were stacked-assembled for powering a smartphone, and four of them were flat-assembled for powering a smartphone. (b) A Miura origami structured paper-like ZIBs with 18 units of paper-like ZIBs for powering a temperature and humidity sensor. (c) Series connection of three flexible paper-like ZIBs as a wristband to power a heart rate monitoring system (schematic diagram, real product diagram and output signal).

Movie S3, ESI†). In addition, we designed a heart rate monitoring system powered by the paper-like ZIBs, schematically depicted in Fig. 6(c). This system can transmit real-time heart rate signals through a Bluetooth module, with the data recorded and analyzed using dedicated software. The panoramic view of the real-time heart rate monitoring system and the real-time exported heart rate signal are depicted in Fig. 6(c). These results underscore the excellent safety and reliability of the Zn||C-PVA/PAN||$NH_4V_4O_{10}$ paper-like batteries in complex deformations, demonstrating their significant potential for portable and wearable electronics.

3. Conclusion

In conclusion, we have successfully engineered an ultra-thin C-PVA/PAN hydrogel electrolyte with dual hydrophobic–hydrophilic polymer networks *via* hydrophobic–hydrophilic phase stabilization strategy. The thickness of hydrogel electrolyte is merely 20 μm, while the corresponding Zn||C-PVA/PAN||$NH_4V_4O_{10}$ paper-like battery is 82 μm. The ZIBs exhibited excellent electrochemical performance, with a specific capacity of 501 mA h g^{-1} at 0.1 A g^{-1} and 180 mA h g^{-1} after 3000 cycles at 20 A g^{-1}. The paper-like battery, employing the Miura folding technique, can increase the areal energy density up to 18 times. This work not only demonstrates a facile strategy to develop an amphiphilic hydrogel structure with dual hydrophobic–hydrophilic polymer networks, but also provides a new pathway to design ultra-thin flexible batteries.

4. Experimental section

4.1 Materials

Polyacrylonitrile (PAN), polyvinyl alcohol (PVA), epichlorohydrin (ECH, 99.6%), and ammonium metavanadate (NH_4VO_3, 99%) were purchased from Macklin and used without purification.

N-Methylpyrrolidone (NMP) and dimethyl sulfoxide (DMSO) were purchased from Aladdin. Zinc trifluoromethanesulfonate ($ZnOTf_2$, 98%) were purchased from Energy Chemical. Sodium hydroxide (NaOH) and oxalic acid ($H_2C_2O_4{\cdot}2H_2O$) were purchased from China National Pharmaceutical Group Corporation. Zinc plate (99.99%) was purchased from Chengshuo Metal Materials Co., LTD. Stainless steel mesh was purchased from Hefei Wenghe Metal Materials Co., LTD. Super P was purchased from Feynman Biotechnology Tech Co., Ltd. Polyvinylidene fluoride (PVDF) was purchased from Nanjing Moges Energy Technology Co., LTD. Carbon cloth was purchased from Nanjing XFNANO Material Technology Co., Ltd.

4.2 Materials preparation

Synthesis of the P-PVA/PAN film. Firstly, 0.916 g PAN and 0.916 g PVA were added to 15 mL DMSO solution and subjected to magnetic stirring for 24 h to obtain the PVA/PAN/DMSO electrospinning solution. Next, the spinning solution was transferred to a 5 mL plastic syringe with a metal nozzle (22G). A voltage of +20 kV was applied to the nozzle, and −0.5 kV was applied to the collector plate. The syringe feeding rate was set at 1 mL h^{-1}. Finally, P-PVA/PAN were collected on a drum covered with silicon release paper.

Synthesis of the C-PVA/PAN hydrogel electrolyte. The 5 mL of ECH was magnetically stirred and evenly dispersed in 100 mL of 6 M NaOH solution at 60 °C. The C-PVA/PAN hydrogel was formed by immersing the P-PVA/PAN film in this solution for 24 hours. Subsequently, the C-PVA/PAN hydrogel was soaked in deionized water to remove excess NaOH. C-PVA/PAN hydrogel electrolyte can be obtained by soaking 2 M $ZnOTf_2$ solution for 24 h after drying C-PVA/PAN hydrogel.

Optimization of C-PVA/PAN hydrogel electrolyte. Mass ratios of PVA to PAN of 3 : 1, 2 : 1, 1 : 1, 1 : 2, and 1 : 3 were tested the mechanical properties and ionic conductivity for. As shown in Fig. S17 (ESI†), as the PVA/PAN ratio increases, the ionic conductivity gradually improves, while the mechanical properties decrease with the increase in PVA. Regarding mechanical properties, this is due to two factors: first, PAN forms a rigid network with inherently better mechanical properties than PVA fibers. Second, the crosslinking effect of ECH directly acts on the PVA fibers. With an increase in PVA and constant ECH crosslinker content, the crosslinking density of the PVA network decreases, leading to reduced mechanical strength. In terms of ion transport, the hydrophilic PVA network has better ion transport capabilities compared to the hydrophobic PAN network. Therefore, increasing the PVA content enhances the ionic conductivity of the hydrogel. Considering both mechanical properties and ionic transport performance, this manuscript uses a PVA mass ratio of 1 : 1.

Synthesis of $NH_4V_4O_{10}$. In the $NH_4V_4O_{10}$ synthesis procedure,[36] 2.340 g NH_4VO_3, was dissolved in 80 mL 80 °C deionized water, Subsequently, 3.782 g $H_2C_2O_4{\cdot}2H_2O$ solid powders were added to the solution. The resulting solution was then transferred to a 100 mL autoclave and maintained in an oven at 140 °C for 48 hours. After cooling the sample to room temperature naturally, the products were collected and subjected to repeated washing with deionized water. Finally, the obtained $NH_4V_4O_{10}$ product was dried at 80 °C for 24 hours.

4.3 Preparation of Zn||$NH_4V_4O_{10}$ batteries

Preparation of the $NH_4V_4O_{10}$ electrodes. The working electrode was prepared by mixing the active material $NH_4V_4O_{10}$ (70 wt%), Super P (20 wt%), and PVDF (10 wt%) in NMP to create a uniform slurry using a planetary centrifugal mixer at 35 Hz for 30 minutes. Subsequently, the slurry was dispersed in NMP to form a homogeneous dispersion solution. This solution was then uniformly coated onto a stainless steel mesh current collector with a thickness of 50 μm and dried overnight at 110 °C in an oven. The mass loading of the active material was approximately 1.0 mg cm^{-2}.

Preparation of the Zn||Zn coin cells. The Zn||Zn coin cells (CR2025, Canrd) were assembled with two 20-microns thick zinc foil electrodes and P-PVA/PAN or C-PVA/PAN hydrogel as the electrolyte and separator. The coin cells were sealed with sealing machine in air, applying pressure until the pressure gauge reached 45 kg cm^{-2}, and held under pressure for 5 min.

Preparation of the paper-like Zn||$NH_4V_4O_{10}$ batteries. The $NH_4V_4O_{10}$@stainless steel mesh, with dimensions of 3 × 3 cm, was used as the cathode in the flexible Zn|| $NH_4V_4O_{10}$ batteries, while the zinc foil, whereas the anode consisted of zinc foil measuring 1 × 2 cm with a thickness of 10 microns. P-PVA/PAN or C-PVA/PAN was utilized as the electrolyte and separator. These components were assembled into a sandwich-like flexible structure in ambient air. Finally, after heat sealing with the polyethylene composite film, the paper-like battery can be obtained.

4.4 Material characterizations

The microstructure and morphology were examined using Siron FEI SEM. Fourier transform infrared (FTIR) analysis was performed with the Thermo Scientific Nicolet iS10 with an attenuated total reflection accessory. The phases of $NH_4V_4O_{10}$ were identified utilizing a Haoyuan DX-2700BH powder X-ray diffractometer with Cu-Kα radiation (λ = 1.5406 Å), and the data were analyzed using MDI Jade software. Tensile and puncture tests were performed using an MTS Systems Corporation Model E43 Tester. The puncture fixture, custom-made by Jinan Huifeng Company, has an upper pressing point with an end face radius of 0.5 mm. Both the tensile and puncture rates were set to 20 mm min^{-1}. Laser confocal microscope images were captured using the KEYENCE VK-X150. *In situ* optical observation of zinc deposition was conducted using the Leica S9i microscope.

4.5 Electrochemical measurements

The electrochemical performances were assessed within the voltage range of 0.2–1.6 V *versus* Zn/Zn^{2+} with a Neware battery test system (MIHW-200-160, Shenzhen, China). Electrochemical impedance spectroscopy (EIS) measurements spanning from 100 kHz to 10 mHz were carried out utilizing a Biologic workstation VSP.

To determine the ionic conductivity of the hydrogel electrolyte, the hydrogel electrolyte film was placed into a stainless-steel mold, and an electrochemical impedance spectroscopy (EIS) test was conducted. The conductivity was calculated using the following equation:

$$\sigma = \frac{l}{RA} \quad (1)$$

where l, A, and R are the thickness, area, and resistance of the hydrogel electrolyte, respectively.

The ionic conductivity at different temperatures ranging from 30 °C to 60 °C was tested to calculate the electrolyte's activation energy using the Arrhenius equation (eqn (2)):

$$\sigma = \sigma_0 \exp(-E_a/kT) \quad (2)$$

where σ is the conductivity, E_a is the activation energy, k is the Boltzmann constant, and T is the absolute temperature.

The thickness of the hydrogel film was determined by measuring the average difference between the mold thickness before and after adding the hydrogel film through multiple measurements. The thickness was around 20 μm.

Zinc-ion transference number of the hydrogel electrolyte was measured by the potentiostatic polarization method and calculated with the Evans equation (eqn (3)).

$$t_{Zn^{2+}} = \frac{I_s(\Delta V - I_0 R_0)}{I_0(\Delta V - I_s R_s)} \quad (3)$$

where I_0 and I_s represent the currents at the initial and steady states, respectively. R_0 and R_s represent the interfacial resistances before and after polarization, respectively.

The results were obtained by performing EIS before and after chronoamperometry measurements with a biologic workstation VSP. The frequency of EIS ranged from 100 000 to 0.1 Hz with a voltage of 10 mV. The current–time profile was obtained by applying a voltage of 10 mV for 3600 s.

4.6 MD simulation model and simulation

MD simulation on zinc deposition. The modeling system in Fig. 4(c) and (d) consists of the zinc anode in the form of Zn foil. The simulation employs a periodic boundary condition in the X and Y directions, with an orthorhombic simulation cell volume of 100 × 100 × 200 Å^3. To investigate the interactions between the molecules and ions (Zn, PVA, and PAN), the optimized potentials for liquid simulations all atom (OPLS-AA) force field is employed.[86,87] The Lennard-Jones n–m potential energy force field is used for the Zn foils.[88] The simulations are performed using the LAMMPS program in the NVT ensemble,[89] with a target temperature of 300 K. A time step of 1 fs is employed, and the van der Waals and Coulomb interactions are truncated at a cutoff radius of 12 and 18 Å, respectively. The particle–particle particle-mesh method is employed to calculate long-range electrostatic interactions.[90]

To accurately describe the movement of Zn ions within PVA molecules in an aqueous environment under an external electric field, and their subsequent deposition on a zinc electrode, we first constructed a simulation box containing Zn ions, water molecules, and PVA molecules. The interactions within and between the molecules were modeled using different force field functions: the OPLS-AA force field for PVA molecules (LigParGen web server: an automatic OPLS-AA parameter generator for organic ligands.[91] 1.14*CM1A-LBCC: localized bond-charge corrected CM1A charges for condensed-phase simulations), the spc/e force field for water molecules, and a combination of Coulomb interactions with the Lennard-Jones (LJ) potential for the Zn ions, which have a +2 charge. To simulate the barrier effect of surface of the Zn electrode on PVA molecules, we implemented an invisible wall at the ends of the box perpendicular to the direction of the extra electric field. This wall prevents PVA molecules from further movement while allowing Zn ions to pass through. Subsequently, we performed further simulations on the Zn ions that passed through this wall.

In the subsequent stage, we utilized a simulation box of identical dimensions, constructing a crystalline structure of Zn atoms at the bottom of box to represent the Zn electrode surface. The Zn atoms in this region were modeled using the LJ potential. In reality, Zn ions passing through the wall and contacting the Zn electrode are reduced to Zn atoms. Therefore, in our simulation, we directly converted the Zn ions that passed through the wall into Zn atoms. We used the LJ potential to ensure consistency with the substrate's potential function, thereby accurately modeling the deposition process of these Zn atoms on the Zn electrode.

MD simulation on water molecule binding. To compare the absorption of water molecules by P-PVA/PAN and C-PVA/PAN, we constructed molecular dynamics models for both types of molecules in an aqueous environment. The intermolecular and intramolecular interactions of P-PVA/PAN and C-PVA/PAN were described using the OPLS-AA force field, while the SPC/E force field was used for water molecules. We built a periodic simulation box containing either P-PVA/PAN or C-PVA/PAN molecules along with 5000 water molecules. A vacuum layer was placed at one end of the box, permitting only water molecules to enter while excluding P-PVA/PAN or C-PVA/PAN. By applying an external electric field, unabsorbed water molecules were directed into the vacuum layer. These water molecules were then removed in real-time to prevent their re-entry into the simulation box through periodic boundaries. With equal amounts of P-PVA/PAN and C-PVA/PAN, we inferred the differences in their water-binding capacities by counting the remaining water molecules in the solution box.

4.7 Heart rate monitoring system

The wearable heart rate monitor, using cutting-edge technology, seamlessly integrates the Pulse Sensor (SEN-11574) with the ESP32 development board to create a sophisticated health monitoring solution. The Pulse Sensor adeptly collects real-time data from the human body, precisely measuring heart rate fluctuations. This data is transmitted to the ESP32 development board, which operates on flexible and bendable batteries (ZIBs), showcasing an innovative power source. The flexibility of these batteries enables the creation of a wristband that not

only conforms to the contours of the skin but also allows for unique and ergonomic designs.

The ESP32 board serves as the central hub, controlling the entire workflow. Utilizing Bluetooth connectivity, the ESP32 seamlessly links to the Arduino IDE on a laptop. This connection enables the transmission of the collected data to the programming software for further processing. The Arduino IDE, with its user-friendly interface, processes the incoming data and presents the user with a clear and comprehensible visualization of the heart rate information. This dynamic synergy between the Pulse Sensor, ESP32 board, and flexible batteries not only ensures accurate health monitoring but also emphasizes the practicality of wearable technology. The wristband, powered by flexible batteries, symbolizes a harmonious blend of innovation and user comfort, showcasing the immense potential of this wearable heart rate monitor in revolutionizing personal health tracking.

Data availability

The data supporting this article have been included as part of the ESI.† All experiments were carried out in compliance with the relevant laws and with the approval of the Scientific Ethical Committee of the School of Material Science and Engineering, Southeast University. Informed, voluntary consent was obtained from the human subject participating in the experiments.

Conflicts of interest

There are no conflicts to declare.

Acknowledgements

This work is supported by the National Key Research and Development Program of China (no. 2023YFC3009502), National Natural Science Foundation of China (no. 52371134, U23A20574, no. 61704080, and no. 61925103), Natural Science Foundation of Jiangsu Province (BK20231432), Aeronautical Science Foundation of China (2023Z015069001), Open Fund of Key Laboratory for Intelligent Nano Materials and Devices of the Ministry of Education NJ2023002 (INMD-2023M04), the Fundamental Research Funds for the Central Universities, and College Student Innovation and Entrepreneurship Training Program of Jiangsu Province.

References

1 W. Wang, Y. Jiang, D. Zhong, Z. Zhang, S. Choudhury, J.-C. Lai, H. Gong, S. Niu, X. Yan, Y. Zheng, C.-C. Shih, R. Ning, Q. Lin, D. Li, Y.-H. Kim, J. Kim, Y.-X. Wang, C. Zhao, C. Xu, X. Ji, Y. Nishio, H. Lyu, J. B.-H. Tok and Z. Bao, *Science*, 2023, **380**, 735.

2 S. Liang, T. Xie, N. A. Blumenschein, T. Zhou, T. Ersevim, Z. Song, J. Liang, M. A. Susner, B. S. Conner, S.-J. Gong, J.-P. Wang, M. Ouyang, I. Žutić, A. L. Friedman, X. Zhang and C. Gong, *Nat. Electron.*, 2023, **6**, 199.

3 X. Cao, Y. You, D. Sha, H. Xia, H. Wang, J. Zhang, R. Hu, Y. Wei, Z. Bao, Y. Xu, L. Pan, C. Lu, W. He, M. Zhou and Z. Sun, *Adv. Funct. Mater.*, 2023, **33**, 2303275.

4 D. Sha, Y. You, R. Hu, X. Cao, Y. Wei, H. Zhang, L. Pan and Z. Sun, *Adv. Mater.*, 2023, **35**, 2211311.

5 D. Sha, C. Lu, W. He, J. Ding, H. Zhang, Z. Bao, X. Cao, J. Fan, Y. Dou, L. Pan and Z. Sun, *ACS Nano*, 2022, **16**, 2711.

6 J.-Q. Huang, X. Guo, X. Lin, Y. Zhu and B. Zhang, *Research*, 2019, **2019**, 2635310.

7 Z. Wang, S. Wang, L. Zhang, H. Liu and X. Xu, *Research*, 2024, **7**, 0298.

8 H. Lu, J. Hu, X. Wei, K. Zhang, X. Xiao, J. Zhao, Q. Hu, J. Yu, G. Zhou and B. Xu, *Nat. Commun.*, 2023, **14**, 4435.

9 Q. Xie, C. Yi, H. Zhang, H. Xia, G. Xu, C. Miao, L. Yang, T. Shui, W. Zhang and Z. Sun, *Adv. Energy Mater.*, 2024, **14**, 2303592.

10 C. Liu, W. Xu, C. Mei, M. Li, W. Chen, S. Hong, W.-Y. Kim, S. Lee and Q. Wu, *Adv. Energy Mater.*, 2021, **11**, 2003902.

11 S. Huang, F. Wan, S. Bi, J. Zhu, Z. Niu and J. Chen, *Angew. Chem., Int. Ed.*, 2019, **58**, 4313.

12 H. Xia, G. Xu, X. Cao, C. Miao, H. Zhang, P. Chen, Y. Zhou, W. Zhang and Z. Sun, *Adv. Mater.*, 2023, **35**, 2301996.

13 Y. Wang, Q. Li, H. Hong, S. Yang, R. Zhang, X. Wang, X. Jin, B. Xiong, S. Bai and C. Zhi, *Nat. Commun.*, 2023, **14**, 3890.

14 L. Wan, H. Zhang, M. Qu, M. Feng, Z. Shang, R. Wang, D. Lei and Y. Cui, *Energy Storage Mater.*, 2023, **63**, 102982.

15 W. Zhang, H. Xia, X. Cao, B. Xu and Z. Li, *Chin. J. Org. Chem.*, 2024, **44**, 148.

16 R. Chen, W. Zhang, Q. Huang, C. Guan, W. Zong, Y. Dai, Z. Du, Z. Zhang, J. Li, F. Guo, X. Gao, H. Dong, J. Zhu, X. Wang and G. He, *Nano-Micro Lett.*, 2023, **15**, 81.

17 K. Wu, J. Cui, J. Yi, X. Liu, F. Ning, Y. Liu and J. Zhang, *ACS Appl. Mater. Interfaces*, 2022, **14**, 34612.

18 Y. Hu, N. Dunlap, S. Wan, S. Lu, S. Huang, I. Sellinger, M. Ortiz, Y. Jin, S. Lee and W. Zhang, *J. Am. Chem. Soc.*, 2019, **141**, 7518.

19 M. Sun, G. Ji and J. Zheng, *Chem. Eng. J.*, 2023, **463**, 142535.

20 J. Zhao, J. Gong, G. Wang, K. Zhu, K. Ye, J. Yan and D. Cao, *Chem. Eng. J.*, 2020, **401**, 125456.

21 J.-L. Yang, J. Li, J.-W. Zhao, K. Liu, P. Yang and H. J. Fan, *Adv. Mater.*, 2022, **34**, 2202382.

22 X. Cao, H. Xia and X. Zhao, *Funct. Mater. Lett.*, 2019, **12**, 1930004.

23 X. Xie, J. Li, Z. Xing, B. Lu, S. Liang and J. Zhou, *Natl. Sci. Rev.*, 2023, **10**, nwac281.

24 T. Qin, K. Li, Y. Liu, Z. Xu and C. Gao, *Adv. Energy Mater.*, 2023, **13**, 2300733.

25 T. Qiu, T. Wang, W. Tang, Y. Li, Y. Li, X. Lang, Q. Jiang and H. Tan, *Angew. Chem., Int. Ed.*, 2023, **62**, e202312020.

26 F. Yang, H. Hua, P. Lai, P. Lin, J. Yang, M. Zhang, Y. Yang and J. Zhao, *ACS Appl. Energy Mater.*, 2022, **5**, 10872.

27 S. Wang, J. Xu, W. Wang, G.-J. N. Wang, R. Rastak, F. Molina-Lopez, J. W. Chung, S. Niu, V. R. Feig, J. Lopez, T. Lei, S.-K. Kwon, Y. Kim, A. M. Foudeh, A. Ehrlich,

A. Gasperini, Y. Yun, B. Murmann, J. B.-H. Tok and Z. Bao, *Nature*, 2018, **555**, 83.
28 Y. S. Choi, R. T. Yin, A. Pfenniger, J. Koo, R. Avila, K. Benjamin Lee, S. W. Chen, G. Lee, G. Li, Y. Qiao, A. Murillo-Berlioz, A. Kiss, S. Han, S. M. Lee, C. Li, Z. Xie, Y.-Y. Chen, A. Burrell, B. Geist, H. Jeong, J. Kim, H.-J. Yoon, A. Banks, S.-K. Kang, Z. J. Zhang, C. R. Haney, A. V. Sahakian, D. Johnson, T. Efimova, Y. Huang, G. D. Trachiotis, B. P. Knight, R. K. Arora, I. R. Efimov and J. A. Rogers, *Nat. Biotechnol.*, 2021, **39**, 1228.
29 W. Lu, W. Bai, H. Zhang, C. Xu, A. M. Chiarelli, A. Vázquez-Guardado, Z. Xie, H. Shen, K. Nandoliya, H. Zhao, K. Lee, Y. Wu, D. Franklin, R. Avila, S. Xu, A. Rwei, M. Han, K. Kwon, Y. Deng, X. Yu, E. B. Thorp, X. Feng, Y. Huang, J. Forbess, Z.-D. Ge and J. A. Rogers, *Sci. Adv.*, 2021, **7**, eabe0579.
30 K. Ji, S. Li, Y. Lin, J. Zhang, M. Wang, C. Bai and D. Kong, *ACS Mater. Lett.*, 2023, **5**, 955.
31 Y. Huang, J. Zhang, J. Liu, Z. Li, S. Jin, Z. Li, S. Zhang and H. Zhou, *Mater. Today Energy*, 2019, **14**, 100349.
32 L. Wang, X. Zhang, Y. Xia, X. Zhao, Z. Xue, K. Sui, X. Dong and D. Wang, *Adv. Mater.*, 2019, **31**, 1902381.
33 T. Shui, M. Pan, A. Li, H. Fan, J. Wu, Q. Liu and H. Zeng, *Chem. Mater.*, 2022, **34**, 8613.
34 Z. Cai, Y. Tang, Y. Wei, P. Wang and H. Zhang, *Acta Biomater.*, 2022, **152**, 124.
35 Y. Li, X. Peng, X. Li, H. Duan, S. Xie, L. Dong and F. Kang, *Adv. Mater.*, 2023, **35**, 2300019.
36 Y. Fang, X. Xie, B. Zhang, Y. Chai, B. Lu, M. Liu, J. Zhou and S. Liang, *Adv. Funct. Mater.*, 2022, **32**, 2109671.
37 P. Gajewski and F. Béguin, *ChemSusChem*, 2020, **13**, 1876.
38 J. Guo, Y. Wang, S. Li, Y. Meng, Y. Qin, L. Jiang, H. Huang and L. Shen, *J. Alloys Compd.*, 2023, **967**, 171708.
39 X. Su, D. Hao, X. Xu, X. Guo, Z. Li and L. Jiang, *ACS Appl. Mater. Interfaces*, 2020, **12**, 25316.
40 S. Tan, C. Wang, B. Yang, J. Luo and Y. Wu, *Adv. Mater.*, 2022, **34**, 2206904.
41 X. Hou, B. Huang, L. Zhou, S. Liu, J. Kong and C. He, *Adv. Mater.*, 2023, **35**, 2301532.
42 M. Gosecka, M. Gosecki and D. Jaworska-Krych, *Adv. Funct. Mater.*, 2023, **33**, 2212302.
43 G. Li, Z. Zhao, S. Zhang, L. Sun, M. Li, J. A. Yuwono, J. Mao, J. Hao, J. (Pimm) Vongsvivut, L. Xing, C.-X. Zhao and Z. Guo, *Nat. Commun.*, 2023, **14**, 6526.
44 S. Cui, W. Miao, X. Wang, K. Sun, H. Peng and G. Ma, *ACS Nano*, 2024, **18**, 12355.
45 S. Wang, L. Yu, S. Wang, L. Zhang, L. Chen, X. Xu, Z. Song, H. Liu and C. Chen, *Nat. Commun.*, 2022, **13**, 3408.
46 K. Zhu, J. Luo, D. Zhang, N. Wang, S. Pan, S. Zhou, Z. Zhang, G. Guo, P. Yang, Y. Fan, S. Hou, Z. Shao, S. Liu, L. Lin, P. Xue, G. Hong, Y. Yang and Y. Yao, *Adv. Mater.*, 2024, **36**, 2311082.
47 P. Lin, J. Cong, J. Li, M. Zhang, P. Lai, J. Zeng, Y. Yang and J. Zhao, *Energy Storage Mater.*, 2022, **49**, 172.
48 J. Cao, Y. Sun, D. Zhang, D. Luo, L. Zhang, R. Chanajaree, J. Qin, X. Yang and J. Lu, *Adv. Energy Mater.*, 2024, **14**, 2302770.
49 L. Miao, R. Wang, W. Xin, L. Zhang, Y. Geng, H. Peng, Z. Yan, D. Jiang, Z. Qian and Z. Zhu, *Energy Storage Mater.*, 2022, **49**, 445.
50 Y. Cui, Y. Ding, L. Guo, C. Guo, Y. Liu, Y. Bai, G. Li and K. Wang, *Energy Mater.*, 2023, **3**, 300023.
51 H. Zhang, T. Shui, W. Zhang and Z. Sun, *Energy Storage Mater.*, 2024, **71**, 103595.
52 Z. Wang, M. Zhou, L. Qin, M. Chen, Z. Chen, S. Guo, L. Wang, G. Fang and S. Liang, *eScience*, 2022, **2**, 209.
53 X. Dou, X. Xie, S. Liang and G. Fang, *Sci. Bull.*, 2024, **69**, 833.
54 S. Li, D. Yu, J. Liu, N. Chen, Z. Shen, G. Chen, S. Yao and F. Du, *Adv. Sci.*, 2023, **10**, 2206836.
55 F. Liu, Z. Chen, G. Fang, Z. Wang, Y. Cai, B. Tang, J. Zhou and S. Liang, *Nano-Micro Lett.*, 2019, **11**, 25.
56 Q. He, G. Fang, Z. Chang, Y. Zhang, S. Zhou, M. Zhou, S. Chai, Y. Zhong, G. Cao, S. Liang and A. Pan, *Nano-Micro Lett.*, 2022, **14**, 93.
57 X. Li, L. Ma, Y. Zhao, Q. Yang, D. Wang, Z. Huang, G. Liang, F. Mo, Z. Liu and C. Zhi, *Mater. Today Energy*, 2019, **14**, 100361.
58 L. Li, L. Zhang, W. Guo, C. Chang, J. Wang, Z. Cong and X. Pu, *J. Mater. Chem. A*, 2021, **9**, 24325.
59 Y. Hao, D. Feng, L. Hou, T. Li, Y. Jiao and P. Wu, *Adv. Sci.*, 2022, **9**, 2104832.
60 Y. Deng, Y. Wu, L. Wang, K. Zhang, Y. Wang and L. Yan, *J. Colloid Interface Sci.*, 2023, **633**, 142.
61 J. Liu, J. Long, Z. Shen, X. Jin, T. Han, T. Si and H. Zhang, *Adv. Sci.*, 2021, **8**, 2004689.
62 N. Zhang, M. Jia, Y. Dong, Y. Wang, J. Xu, Y. Liu, L. Jiao and F. Cheng, *Adv. Funct. Mater.*, 2019, **29**, 1807331.
63 Z. Liu, D. Wang, Z. Tang, G. Liang, Q. Yang, H. Li, L. Ma, F. Mo and C. Zhi, *Energy Storage Mater.*, 2019, **23**, 636.
64 Y. Lu, Z. Wang, M. Li, Z. Li, X. Hu, Q. Xu, Y. Wang, H. Liu and Y. Wang, *Adv. Funct. Mater.*, 2024, **34**, 2310966.
65 H. Zhang, X. Gan, Z. Song and J. Zhou, *Angew. Chem., Int. Ed.*, 2023, **62**, e202217833.
66 Z. Li, G. Zhou, L. Ye, J. He, W. Xu, S. Hong, W. Chen, M.-C. Li, C. Liu and C. Mei, *Chem. Eng. J.*, 2023, **472**, 144992.
67 J. Feng, D. Ma, K. Ouyang, M. Yang, Y. Wang, J. Qiu, T. Chen, J. Zhao, B. Yong, Y. Xie, H. Mi, L. Sun, C. He and P. Zhang, *Adv. Funct. Mater.*, 2022, **32**, 2207909.
68 C. Fu, Y. Wang, C. Lu, S. Zhou, Q. He, Y. Hu, M. Feng, Y. Wan, J. Lin, Y. Zhang and A. Pan, *Energy Storage Mater.*, 2022, **51**, 588.
69 B. Zhang, L. Qin, Y. Fang, Y. Chai, X. Xie, B. Lu, S. Liang and J. Zhou, *Sci. Bull.*, 2022, **67**, 955.
70 Z. Shen, Z. Tang, C. Li, L. Luo, J. Pu, Z. Wen, Y. Liu, Y. Ji, J. Xie, L. Wang, Y. Yao and G. Hong, *Adv. Energy Mater.*, 2021, **11**, 2102055.
71 X. Zhao, L. Mao, Q. Cheng, F. Liao, G. Yang and L. Chen, *Carbon*, 2022, **186**, 160.
72 J. Cong, X. Shen, Z. Wen, X. Wang, L. Peng, J. Zeng and J. Zhao, *Energy Storage Mater.*, 2021, **35**, 586.
73 K. Leng, G. Li, J. Guo, X. Zhang, A. Wang, X. Liu and J. Luo, *Adv. Funct. Mater.*, 2020, **30**, 2001317.
74 L. Ma, S. Chen, C. Long, X. Li, Y. Zhao, Z. Liu, Z. Huang, B. Dong, J. A. Zapien and C. Zhi, *Adv. Energy Mater.*, 2019, **9**, 1902446.

75 Y. Cheng, Y. Jiao and P. Wu, *Energy Environ. Sci.*, 2023, **16**, 4561.
76 Y. Meng, L. Zhang, M. Peng, D. Shen, C. Zhu, S. Qian, J. Liu, Y. Cao, C. Yan, J. Zhou and T. Qian, *Adv. Funct. Mater.*, 2022, **32**, 2206653.
77 H. Lu, J. Hu, L. Wang, J. Li, X. Ma, Z. Zhu, H. Li, Y. Zhao, Y. Li, J. Zhao and B. Xu, *Adv. Funct. Mater.*, 2022, **32**, 2112540.
78 M. Chen, J. Chen, W. Zhou, X. Han, Y. Yao and C.-P. Wong, *Adv. Mater.*, 2021, **33**, 2007559.
79 X. Xiao, X. Xiao, Y. Zhou, X. Zhao, G. Chen, Z. Liu, Z. Wang, C. Lu, M. Hu, A. Nashalian, S. Shen, K. Xie, W. Yang, Y. Gong, W. Ding, P. Servati, C. Han, S. X. Dou, W. Li and J. Chen, *Sci. Adv.*, 2021, **7**, eabl3742.
80 S. Ji, J. Qin, S. Yang, P. Shen, Y. Hu, K. Yang, H. Luo and J. Xu, *Energy Storage Mater.*, 2023, **55**, 236.
81 F. Wang, J. Zhang, H. Lu, H. Zhu, Z. Chen, L. Wang, J. Yu, C. You, W. Li, J. Song, Z. Weng, C. Yang and Q.-H. Yang, *Nat. Commun.*, 2023, **14**, 4211.
82 L. Li, S. Liu, W. Liu, D. Ba, W. Liu, Q. Gui, Y. Chen, Z. Hu, Y. Li and J. Liu, *Nano-Micro Lett.*, 2021, **13**, 1.
83 Y. Bai, H. Zhang, Q. Hu, Y. Zhou and B. Xiang, *Nano Energy*, 2021, **90**, 106596.
84 K. H. Shin, D. Ji, J. M. Park, Y. S. Joe, H. S. Park and J. Kim, *Adv. Funct. Mater.*, 2024, **34**, 2309048.
85 G. Cao, L. Zhao, X. Ji, Y. Peng, M. Yu, X. Wang, X. Li and F. Ran, *Small*, 2023, **19**, 2207610.
86 J. N. Canongia Lopes and A. A. H. Pádua, *J. Phys. Chem. B*, 2004, **108**, 16893.
87 J. N. Canongia Lopes, J. Deschamps and A. A. H. Pádua, *J. Phys. Chem. B*, 2004, **108**, 2038.
88 S. Zhen and G. J. Davies, *Phys. Status Solidi A*, 1983, **78**, 595.
89 S. Plimpton, *J. Comput. Phys.*, 1995, **117**, 1.
90 Z. Cheng, K. Wang, J. Fu, F. Mo, P. Lu, J. Gao, D. Ho, B. Li and H. Hu, *Adv. Energy Mater.*, 2024, **14**, 2304003.
91 L. S. Dodda, I. Cabeza de Vaca, J. Tirado-Rives and W. L. Jorgensen, *Nucleic Acids Res.*, 2017, **45**, W331.

